

Article

Enhanced Energy Storage Performance and Efficiency in $\text{Bi}_{0.5}(\text{Na}_{0.8}\text{K}_{0.2})_{0.5}\text{TiO}_3\text{-Bi}_{0.2}\text{Sr}_{0.7}\text{TiO}_3$ Relaxor Ferroelectric Ceramics via Domain Engineering

Srinivas Pattipaka ¹, Hyunsu Choi ¹, Yeseul Lim ¹, Kwi-Il Park ², Kyeongwoon Chung ³
and Geon-Tae Hwang ^{1,*}

¹ Department of Materials Science and Engineering, Pukyong National University, 45 Yongso-ro, Nam-Gu, Busan 48513, Republic of Korea; cnuphy444@gmail.com (S.P.); sky5021184@pukyong.ac.kr (H.C.)

² School of Materials Science and Engineering, Kyungpook National University, 80 Daehak-ro, Buk-Gu, Daegu 41566, Republic of Korea; kipark@knu.ac.kr

³ Department of Biofibers and Biomaterials Science, Kyungpook National University, Daegu 41566, Republic of Korea; kychung@knu.ac.kr

* Correspondence: gthwang@pknu.ac.kr

Abstract: Dielectric materials are highly desired for pulsed power capacitors due to their ultra-fast charge-discharge rate and excellent fatigue behavior. Nevertheless, the low energy storage density caused by the low breakdown strength has been the main challenge for practical applications. Herein, we report the electric energy storage properties of $(1 - x)\text{Bi}_{0.5}(\text{Na}_{0.8}\text{K}_{0.2})_{0.5}\text{TiO}_3\text{-}x\text{Bi}_{0.2}\text{Sr}_{0.7}\text{TiO}_3$ (BNKT-BST; $x = 0.15\text{--}0.50$) relaxor ferroelectric ceramics that are enhanced via a domain engineering method. A rhombohedral-tetragonal phase, the formation of highly dynamic PNRs, and a dense microstructure are confirmed from XRD, Raman vibrational spectra, and microscopic investigations. The relative dielectric permittivity (2664 at 1 kHz) and loss factor (0.058) were gradually improved with BST ($x = 0.45$). The incorporation of BST into BNKT can disturb the long-range ferroelectric order, lowering the dielectric maximum temperature T_m and inducing the formation of highly dynamic polar nano-regions. In addition, the T_m shifts toward a high temperature with frequency and a diffuse phase transition, indicating relaxor ferroelectric characteristics of BNKT-BST ceramics, which is confirmed by the modified Curie-Weiss law. The rhombohedral-tetragonal phase, fine grain size, and lowered T_m with relaxor properties synergistically contribute to a high P_{max} and low P_r , improving the breakdown strength with BST and resulting in a high recoverable energy density W_{rec} of 0.81 J/cm^3 and a high energy efficiency η of 86.95% at 90 kV/cm for $x = 0.45$.

Keywords: lead-free ceramic capacitors; dielectric; relaxor ferroelectric; domain engineering; energy storage



Citation: Pattipaka, S.; Choi, H.; Lim, Y.; Park, K.-I.; Chung, K.; Hwang, G.-T. Enhanced Energy Storage Performance and Efficiency in $\text{Bi}_{0.5}(\text{Na}_{0.8}\text{K}_{0.2})_{0.5}\text{TiO}_3\text{-Bi}_{0.2}\text{Sr}_{0.7}\text{TiO}_3$ Relaxor Ferroelectric Ceramics via Domain Engineering. *Materials* **2023**, *16*, 4912. <https://doi.org/10.3390/ma16144912>

Academic Editor: Laurent Daniel

Received: 5 June 2023

Revised: 1 July 2023

Accepted: 7 July 2023

Published: 9 July 2023



Copyright: © 2023 by the authors. Licensee MDPI, Basel, Switzerland. This article is an open access article distributed under the terms and conditions of the Creative Commons Attribution (CC BY) license (<https://creativecommons.org/licenses/by/4.0/>).

1. Introduction

Materials with high energy and power have received extensive attention for high-power applications, such as microwaves, electromagnetic devices, pulsed power devices, hybrid electric vehicles, high-frequency inverters, and other energy storage devices [1–3]. In particular, dielectric ceramics are the most promising materials for energy storage applications due to their super-fast charge-discharge rate and excellent temperature stability compared to electrochemical energy storage devices (batteries and electrochemical capacitors) and dielectric polymers [4–6]. However, the dielectric capacitor's energy storage density and efficiency are much lower than those of polymers/batteries due to their low dielectric breakdown strength (DBS), which restricts their practical application in energy storage devices.

The recoverable energy density (W_{rec}) of a dielectric capacitor is governed by the applied electric field (E) and induced polarization (P), expressed by the following equation,

usually estimated from the P - E loop, and it is schematically shown in Figure 1a by the shaded area with cyan color [7–10].

$$W_{rec} = \int_{P_r}^{P_{max}} E dP \quad (1)$$

where P_{max} and P_r are the maximum polarization and remnant polarization, respectively (Figure 1a). Energy efficiency (η) can be estimated by the following equation [8–10].

$$\eta = \frac{W_{rec}}{W_{rec} + W_{loss}} \quad (2)$$

where W_{loss} is the hysteresis loss. According to Equation (1), the energy storage properties can be significantly enhanced by increasing the difference between P_r and P_{max} (ΔP). The breakdown electric field (E_{BD}) is also an essential factor for energy storage; i.e., a higher DBS is responsible for a large energy storage density.

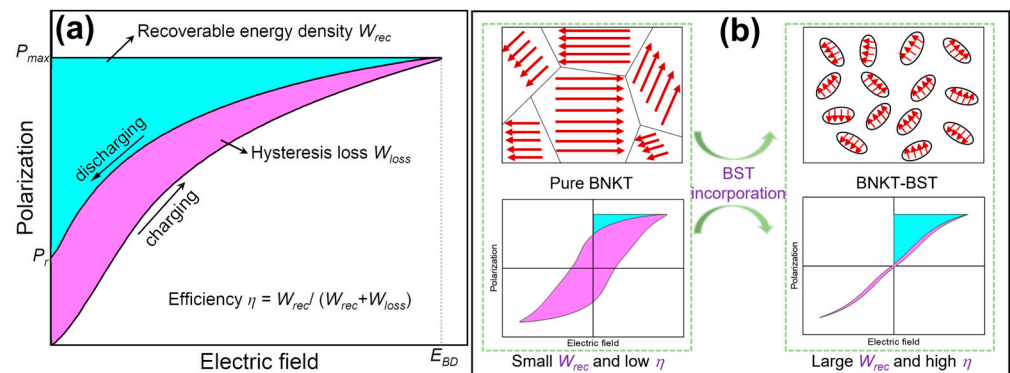


Figure 1. Schematic diagram of (a) recoverable energy density and hysteresis loss from P - E hysteresis loop of a dielectric material. (b) Domain evolution and formation of FE to RFE transition with the substitution of BST into BNKT, resulting in enhanced W_{rec} and η .

Linear dielectrics (LDEs), ferroelectrics (FEs), relaxor ferroelectrics (RFEs), and anti-ferroelectrics (AFE) have been widely explored for electrostatic energy storage applications [11]. LDEs (Al_2O_3 and SrTiO_3) typically show low relative dielectric permittivity and loss factor, high E_{BD} , and free hysteresis loop with low polarization, resulting in poor W_{rec} and high η [11–13]. The AFEs (PbZrO_3 , PbHfO_3 , AgNbO_3 , and NaNbO_3) display elevated polarization and substantial hysteresis because of phase transition between AFE and FE phases induced by the external field, leading to extremely high W_{rec} and low η [14–18]. The RFEs ($\text{Bi}_{0.5}\text{Na}_{0.5}\text{TiO}_3$ (BNT), BaTiO_3 (BT), and BiFeO_3 (BFO)) display moderate P_{max} and small P_r (Figure 1b), arising from widespread PNRs, which generally exhibit highly dynamic short-range FE orders. However, these PNRs gradually transform into long-range FE orders with an increasing field, resulting in large P_{max} . After eliminating the electric field, the induced FE orders will easily revert to PNRs, leading to small P_r [19–22]. Hence, the RFEs usually show high W_{rec} and η . Therefore, lead-based RFE materials have been widely investigated for energy storage applications [23,24]. However, lead is hazardous to the environment and human health due to its toxicity, which has motivated the development of alternative lead-free materials. In recent years, lead-free perovskite-structured (ABO_3) RFEs, such as BT [25–27], BNT [6,28–31], BFO [32–34], and other lead-free perovskite RFEs, such as $\text{Bi}_4\text{Ti}_3\text{O}_{12}$ [35], $\text{Sr}_{1.25}\text{Bi}_{2.75}\text{Nb}_{1.25}\text{Ti}_{1.75}\text{O}_{12}$ [36], and $\text{Sr}_{0.6}\text{Ba}_{0.4}\text{Nb}_2\text{O}_6$ [37] based materials with boosted energy storage performance, have been reported for applications in energy storage devices.

Perovskite-structured BNT-based ceramics exhibit a strong ferroelectric response, since Bi^{3+} has a lone pair of electrons ($6s^2$), which strongly hybridizes with the oxygen 2p orbital [38]. Furthermore, the formation of highly dynamic polar nano-regions (PNRs) are

facilitated by local random fields induced by valency differences and compositional inhomogeneity [39,40]. Moreover, the relaxor behavior of the material can be improved by adding another phase with a similar perovskite to form a solid solution or modifying the base compound with a suitable dopant, which enables slim P - E loops [41]. Sayyed et al. [42] investigated the local structural deformation and dielectric anomalies near the morphotropic phase boundary (MPB) of $(1 - x) \text{Na}_{0.5}\text{Bi}_{0.5}\text{TiO}_3$ - $x\text{SrTiO}_3$ ceramics. The ferroelectric response of $(1 - x) \text{Na}_{0.5}\text{Bi}_{0.5}\text{TiO}_3$ - SrTiO_3 - $x\text{AgNbO}_3$ ceramics is similar to the antiferroelectric response and improved energy storage performance [43]. Shi et al. [44] reported that Zr- and Sm-doped $0.74\text{Na}_{0.5}\text{Bi}_{0.5}\text{TiO}_3$ - 0.26SrTiO_3 ceramics significantly enhanced energy storage performance and the DBS. $\text{Bi}_{0.2}\text{Sr}_{0.7}\text{TiO}_3$ (BST) exhibits strong polarization and a wide-phase transition temperature with diffused dielectric maxima. It was incorporated into BNT ceramics, suppressing the field-generated ferroelectric phase and achieving a large P_{max} and small P_r [45,46]. Recently, Li et al. reported a synergistic approach to enhance the energy storage response in BNT-based RFEs by introducing PNRs and lowering the transition temperature by stabilizing the AFE responses at low temperatures [9].

In this work, we investigate a domain engineering process to improve the energy storage performance by modifying $\text{Bi}_{0.5}(\text{Na}_{0.8}\text{K}_{0.2})_{0.5}\text{TiO}_3$ (BNKT) RFEs with BST, since $\text{Bi}_{0.5}(\text{Na}_{1-x}\text{K}_x)_{0.5}\text{TiO}_3$ exhibits a stronger ferroelectric response with relaxor behavior at the MPB at $x = 0.16$ – 0.2 [47,48] than pure BNT. It is revealed that the addition of BST can disturb the long-range ferroelectric order and transform the ferroelectric microdomains of BNKT into highly dynamic PNRs. This results in a macroscopic ferroelectric to relaxor ferroelectric transition, as schematically illustrated in Figure 1b. The favorable relaxor ferroelectric state formed by the domain engineering method simultaneously produces a large P_{max} and reduced P_r , which facilitates the enhancement in DBS with the BST, resulting in high energy density and high efficiency of the BNKT-BST RFEs.

2. Materials and Methods

$(1 - x) \text{Bi}_{0.5}(\text{Na}_{0.8}\text{K}_{0.2})_{0.5}\text{TiO}_3$ - $x\text{Bi}_{0.2}\text{Sr}_{0.7}\text{TiO}_3$ (BNKT-BST; $x = 0.15, 0.30, 0.40, 0.45,$ and 0.50) RFE ceramics were fabricated via a conventional solid-state reaction method. To prepare BNKT and BST, high-purity raw materials of Bi_2O_3 (Sigma-Aldrich, St. Louis, MI, USA, 99.9%), Na_2CO_3 (Sigma-Aldrich, St. Louis, MI, USA, 99.5%), K_2CO_3 (Sigma-Aldrich, St. Louis, MI, USA, 99%), TiO_2 (Sigma-Aldrich, St. Louis, MI, USA, 99%), and SrCO_3 (Sigma-Aldrich, St. Louis, MI, USA, 98%) were weighed according to the nominal stoichiometric compositions and then ball-milled using a planetary ball mill for 24 h with ZrO_2 balls in ethanol. After the slurries were dried at 120°C , the mixture of BNKT and BST powders was calcined at 800°C and 950°C for 2 h and 3 h, respectively, to form a pure phase of $\text{Bi}_{0.5}(\text{Na}_{0.8}\text{K}_{0.2})_{0.5}\text{TiO}_3$ and $\text{Bi}_{0.2}\text{Sr}_{0.7}\text{TiO}_3$. Both BNKT and BST calcined powders were mixed and ball-milled for 12h to prepare a BNKT-BST composition. Further, these powders were granulated with 5 wt.% polyvinyl alcohol (Sigma-Aldrich, 99%, St. Louis, MI, USA,) and uniaxially pressed into disks, at a pressure of 10 MPa, of 10 mm diameter and ~ 0.5 mm thickness, followed by sintering at 1100°C for 3 h. To perform electrical measurements, a silver paste (ELCOAT, Electroconductives) was coated on both sides of the sintered disks.

The phase formation of the BNKT-BST ceramic samples was examined using an X-ray diffractometer (Rigaku, Tokyo, Japan, TTRAX III 18 kW) with monochromatic $\text{Cu-K}\alpha$ radiation ($\lambda = 1.5406 \text{ \AA}$). Raman spectra were recorded using a Raman spectrometer (JOBIN YVON, Oberursel, Germany, LABRAM HR800) with a laser wavelength of 532.06 nm. Surface morphology was investigated using a field emission scanning electron microscope (FESEM) (JEOL, Tokyo, Japan, JSM-7610F). Temperature- and frequency-dependent dielectric properties were measured from room temperature (RT) to 450°C and 1 kHz–1 MHz using an impedance analyzer (Hewlett Packard, Palo Alto, CA, USA, 4294A). P - E , I - E loops, and fatigue behavior were measured using a ferroelectric tester (AixACCT Systems GmbH, Aachen, Germany, TF Analyzer 2000).

3. Results and Discussion

3.1. Phase Evolution and Microstructure

Figure 2a shows the X-ray diffraction (XRD) patterns of BNKT-BST ceramics ($x = 0.15\text{--}0.50$) in the 2θ range of $20\text{--}70^\circ$. All of the samples revealed a rhombohedral and tetragonal crystal structure, indicating the diffusion of BST into BNKT and the formation of BNKT-BST as a homogeneous solid solution. At RT, the BNKT system exhibits a rhombohedral and tetragonal crystal structure near MPB at $x = 0.16\text{--}0.2$ [47,48]. The formation of MPB in BNKT-BST ceramics is confirmed by the splitting of the (021)/(111) and (122)/(211) peaks at 2θ around 40° and 58° , respectively, which is shown in Figure 2b. Similar splitting and formation of MPB were observed in $\text{Bi}_{0.5}(\text{Na}_{1-x}\text{K}_x)_{0.5}\text{TiO}_3\text{-BiAlO}_3$ [49], $\text{Bi}_{0.5}\text{Na}_{0.5}\text{TiO}_3\text{-Bi}_{0.5}\text{K}_{0.5}\text{TiO}_3\text{-Bi}_{0.5}\text{Li}_{0.5}\text{TiO}_3$ [50], and $(\text{Bi}_{0.5}\text{Na}_{0.5})\text{TiO}_3\text{-(Bi}_{0.5}\text{K}_{0.5})\text{TiO}_3\text{-BaTiO}_3$ [51] ceramics. In addition, both the (021) and (122) peaks shifted slightly toward lower angles with increasing BST into BNKT, demonstrating enhanced lattice parameters (Figure 2b). The enhancement in lattice parameters can be attributed to the ionic radius of Sr^{2+} (1.44 Å), which is larger than that of Bi^{3+} (1.36 Å), Na^+ (1.39 Å), and K^+ (1.38 Å), respectively, at the A-site [52–54].

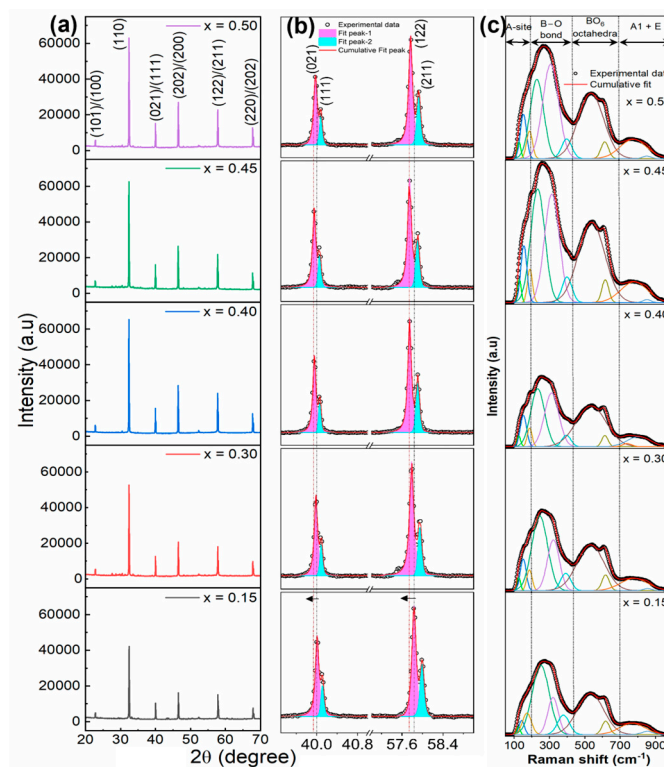


Figure 2. (a) XRD patterns of the $(1 - x)\text{BNKT-xBST}$ ceramics for $x = 0.15\text{--}0.50$, where (b) $2\theta = 39\text{--}59^\circ$. (c) Raman spectra of BNKT-BST ceramics along with spectral deconvolution.

Figure 2c shows the Raman spectra of BNKT-BST along with spectral de-convolution in the Raman shift of $50\text{--}1000\text{ cm}^{-1}$. The Raman spectra of all compositions are similar to the previous reports of BNKT-based ceramics [51,55]. The Raman active bands are divided into four Raman vibration modes, as shown at the top of Figure 2c. (i) The modes below 200 cm^{-1} are related to the vibration of the A-site (Bi-O, Na-O, K-O, and Sr-O); (ii) the modes between 200 and 440 cm^{-1} correspond to the vibrations of B-O (Ti-O); (iii) the modes between 440 and 700 cm^{-1} correspond to the vibrations of BO_6 (TiO_6)-octahedra; and (iv) the modes above 700 cm^{-1} are related to the $A1$ and E (longitudinal optical) overlapping modes [55]. The modes appearing at $124\text{--}172\text{ cm}^{-1}$ and 768 cm^{-1} are shifted to the higher wavenumbers of $128\text{--}189\text{ cm}^{-1}$ and 779 cm^{-1} with BST, associated with the A-site and $A1 + E$ vibrations caused by A-site disorder. Such a disorder is induced by the incorporation of BST (Bi^{3+} and Sr^{2+}) into the BNKT (Bi^{3+} , Na^+ , and K^+) system [56]. In

addition, a noticeable change at 250 and 320 cm^{-1} shifted toward a lower wavenumber of 233 and 305 cm^{-1} with BST, which is caused by an increase in the *B*-site disorder in the BNKT-BST system [53]. Moreover, these modes are slightly broadened, confirming the disturbance of the long-range ferroelectric order and the formation of highly dynamic PNRs, improving the relaxor characteristics of BNKT-BST [44]. This result is consistent with the XRD and electrical properties presented in Sections 3.2 and 3.3.

Figure 3 shows FESEM images of the BNKT-BST ceramics. All of the ceramics display rectangular-shaped grains, which are homogeneously distributed. Figure 3d clearly shows that the $x = 0.45$ composition exhibits a highly dense microstructure and is more compact with smaller grains, as compared to the other samples of BNKT-BST ($x < 0.45$ and $x = 0.50$). To prove that all of the samples are homogeneous and highly dense, the density of sintered BNKT-BST ceramic samples was calculated using the Archimedes principle. It increased with BST from 5.58 g/cm^3 to 5.73 g/cm^3 for $x = 0.15$ to 0.45 and further decreased (5.54 g/cm^3) for $x = 0.50$. The calculated relative density of BNKT-BST ranged from 94.96% to 98.17% of the theoretical density [57], confirming that these samples are homogeneous and highly dense. Further, the average grain size of the BNKT-BST ceramics was estimated using Image-J software (Wayne Rasband and contributors, National Institutes of Health, USA, ImageJ 1.53t) via the linear intercept method and found to be 1.37 μm for the $x = 0.15$ composition; it gradually enhanced to 1.6 μm with the incorporation of BST. Grain size enhancement is caused by the generation of oxygen vacancies by Sr^{2+} entering the perovskite of BNKT and being substituted at the *A*-site of Bi^{3+} , Na^+ , and K^+ [58]. Previous reports have investigated that the fine grain size with a homogeneous and dense microstructure can withstand higher electric fields, leading to high DBS, and improve energy storage performance [59,60].

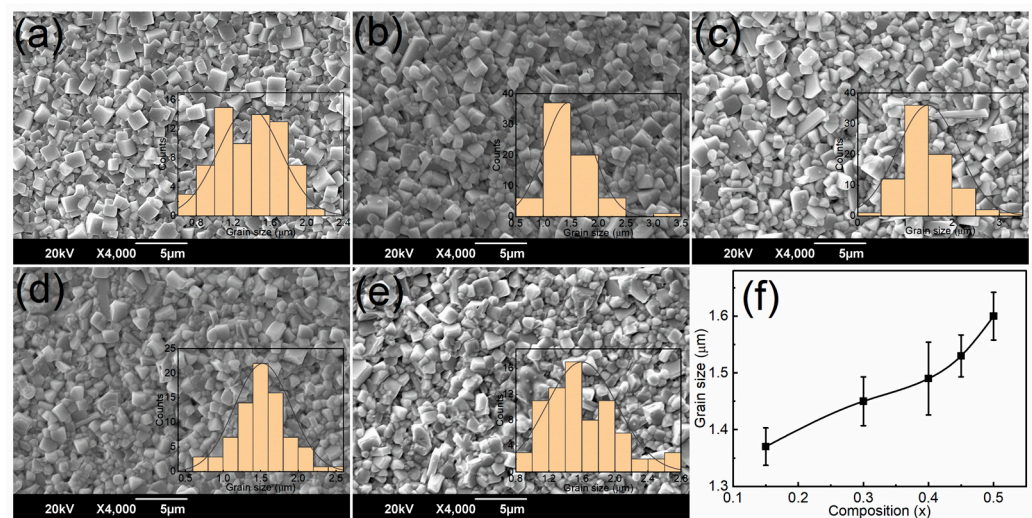


Figure 3. FESEM images of $(1 - x)$ BNKT- x BST ceramics for (a) $x = 0.15$, (b) $x = 0.30$, (c) $x = 0.40$, (d) $x = 0.45$, and (e) $x = 0.50$. The inset of (a–e) shows the average grain size versus counts (grain size distribution histogram). (f) The variation in grain size with composition (x).

3.2. Dielectric Properties and Relaxor Behavior

Figure 4a displays the frequency variation in the relative dielectric permittivity (ϵ_r) (solid line) and loss factor ($\tan \delta$) (dot line) of BNKT-BST ceramic capacitors, measured at RT in the range of 1 kHz to 1 MHz. The sample $x = 0.15$ displayed a higher ϵ_r of 1481 and $\tan \delta$ of 0.231 at 1 kHz than pure BNKT (ϵ_r of 1273 and $\tan \delta$ of 0.047 at 1 kHz), as reported in our previous report [48]. These ϵ_r values gradually enhanced to 2664, and the $\tan \delta$ values reduced to 0.058 for the $x = 0.45$ sample (Figure 4b). The enhancement in the dielectric properties is attributed to the incorporation of BST into BNKT and the dense microstructure.

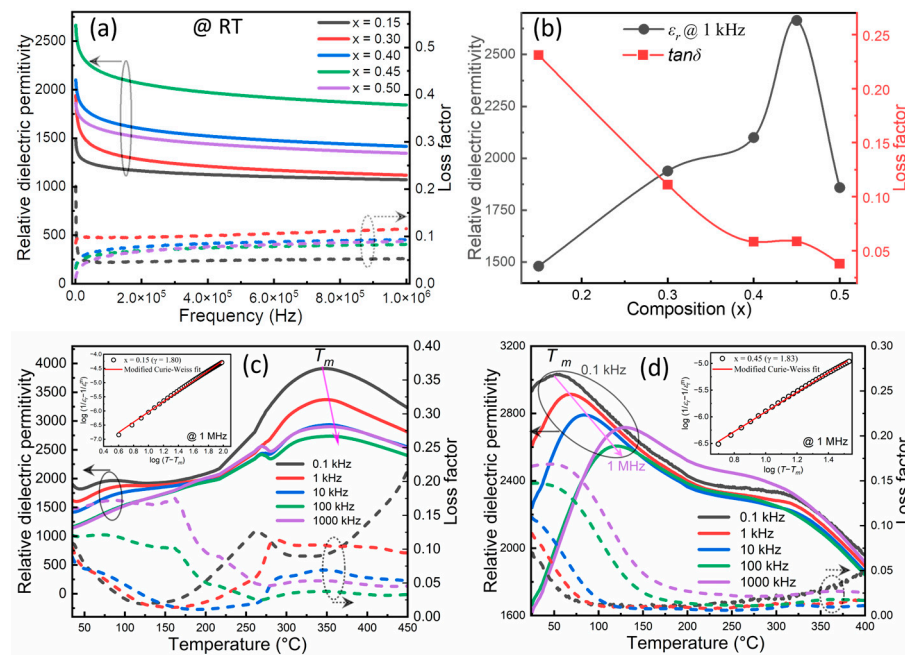


Figure 4. (a) Frequency variation of relative dielectric permittivity and loss factor of BNKT-BST ceramics for $x = 0.15$ – 0.50 . (b) Composition vs. relative dielectric permittivity and loss factor. (c,d) Temperature variation of relative dielectric permittivity and loss factor of BNKT-BST for $x = 0.15$ and 0.45 (The left and right sides of the arrows with circles enclosed by curves indicate relative dielectric permittivity and loss factor, respectively). The inset of (c,d) shows the $\log(T - T_m)$ versus $\log[(1/\epsilon_r) - (1/\epsilon_r^m)]$ of BNKT-BST for $x = 0.15$ and 0.45 , respectively, at 1 MHz.

Figure 4c,d displays the temperature dependence of ϵ_r and $\tan \delta$ of BNKT-BST for the lower and higher compositions ($x = 0.15$ and 0.45), measured at various frequencies (0.1 kHz to 1 MHz). It was observed that the dielectric maximum temperature (T_m) shifted toward a lower temperature 53°C with the incorporation of BST for $x = 0.45$ (Figure 4d), as compared to $x = 0.15$ ($T_m = 345^\circ\text{C}$) (Figure 4c) and pure BNKT (300°C) [48], and this is similar to the $0.74 \text{ Na}_{0.5}\text{Bi}_{0.5}\text{TiO}_3$ - 0.26 SrTiO_3 ceramics reported by Shi et al. [44]. The incorporation of BST into BNKT can disturb the long-range ferroelectric order, resulting in a lowered T_m . This lower T_m leads to the formation of highly dynamic PNRs due to the mismatch of the ionic radius at the A -site of BNKT-BST. In addition, the T_m shifted toward higher temperatures, and dielectric peaks diffused with an increase in frequency. This frequency dispersion with a diffuse phase transition reveals typical relaxor ferroelectric characteristics [61,62]. The degree of the relaxor characteristics was determined using the modified Curie-Weiss law via the following equation [52,63].

$$\left(\frac{1}{\epsilon_r}\right) - \left(\frac{1}{\epsilon_r^m}\right) = (T - T_m)^\gamma / C \quad (3)$$

where ϵ_r^m is the maximum relative dielectric permittivity at the maximum temperature T_m , T is the temperature, γ is the degree of relaxation, and C is the Curie constant. Generally, the γ value is 1 for normal ferroelectrics and between 1 and 2 for relaxor ferroelectrics [63]. The insets of Figure 4c,d show the log-log plots of $(1/\epsilon_r - 1/\epsilon_r^m)$ vs. $(T - T_m)$ of BNKT-BST for $x = 0.15$ and 0.45 , measured at 1 MHz. The value of γ slightly increased from 1.80 to 1.83, proving that there is an increase in relaxor behavior with BST from $x = 0.15$ to 0.45 , leading to an increase in the energy storage performance. This is consistent with Raman's results and previous reports [4–6].

3.3. FE-RFE Transformation, Domain Evolution, and Energy Storage Performance

Figure 5 displays the RT bipolar P - E hysteresis loops and current (I)-electric field (E) curves of BNKT-BST ceramic capacitors measured at various electric fields and 10 Hz. The

BNKT-BST ($x = 0.15$) sample exhibits a typical ferroelectric (FE) characteristic, displaying high remnant polarization P_r of $19.89 \mu\text{C}/\text{cm}^2$, high maximum polarization P_{max} of $31.46 \mu\text{C}/\text{cm}^2$, and a high coercive field E_c of $16.66 \text{ kV}/\text{cm}$. These values, listed in Table 1, gradually decreased, whereas the E_{max} or E_{BD} increased from $57.42 \text{ kV}/\text{cm}$ to $90 \text{ kV}/\text{cm}$ with the incorporation of BST ($x = 0.45$), which is favorable for high energy storage density (Figure 5f). It is evident that the two peaks in the I - E curves ($x \geq 0.30$) and slim P - E loops are attributed to the formation of highly dynamic PNRs, which can commonly be seen in RFEs [64]. In general, the P - E loops present in normal FEs are due to the macroscopic domain wall motion, while in RFEs, highly dynamic PNRs exist instead of macrodomains, resulting in slim P - E loops [19].

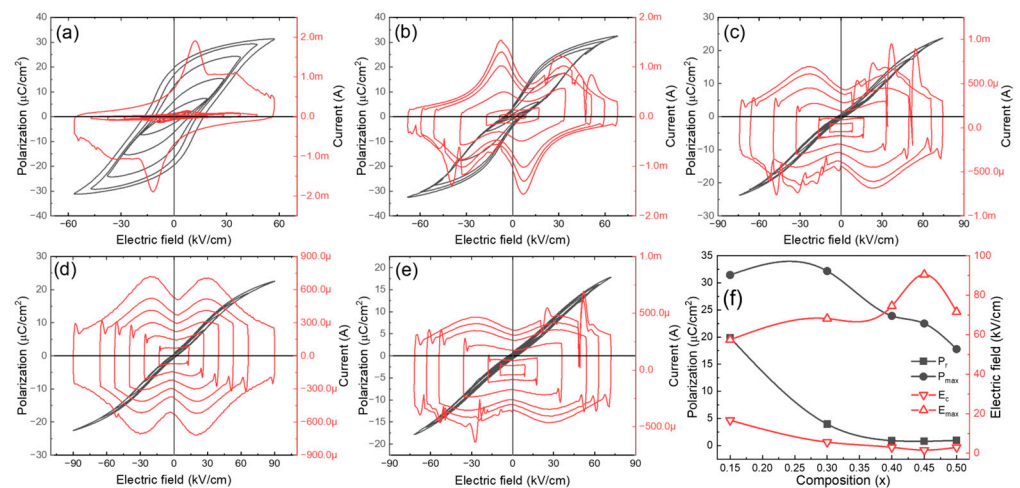


Figure 5. RT P - E and I - E curves of BNKT-BST ceramics for (a) $x = 0.15$, (b) $x = 0.30$, (c) $x = 0.40$, (d) $x = 0.45$, and (e) $x = 0.50$. (f) Composition (x) versus polarization and electric field.

Table 1. List of all values of ferroelectric properties (P_r , P_{max} , E_c , and E_{BD}) and energy storage performance (W_{rec} and η) of BNKT-BST ceramics for $x = 0.15$ – 0.50 .

Composition	P_r ($\mu\text{C}/\text{cm}^2$)	P_{max} ($\mu\text{C}/\text{cm}^2$)	E_c (kV/cm)	E_{BD} (kV/cm)	W_{rec} (J/cm^3)	η (%)
$x = 0.15$	19.89	31.46	16.66	57.42	0.20	18.67
$x = 0.30$	3.95	32.18	5.59	68.18	0.57	52.02
$x = 0.40$	0.92	23.91	2.98	74.57	0.73	85.30
$x = 0.45$	0.78	22.5	1.58	90	0.81	86.95
$x = 0.50$	0.96	17.79	2.94	71.54	0.56	85.23

Further, the W_{rec} was calculated via Equation (1) from P - E loops, which are shown in Figure 6 (cyan shaded area). The W_{loss} is calculated by the enclosed area of the P - E loops in the first quadrant (magenta shaded area), and η is calculated by Equation (2); they are listed in Table 1. The W_{rec} values gradually increased, the W_{loss} values decreased with the substitution of BST, and the composition $x = 0.45$ displays a high energy density of $0.81 \text{ J}/\text{cm}^3$ at an E_{BD} of $90 \text{ kV}/\text{cm}$ and high energy efficiency of 86.95% (Figure 6f). The improvement in the energy storage performance is achieved via the domain engineering method by modifying BNKT with BST. It can be understood that the substitution of BST can transform the ferroelectric microdomains of BNKT into highly dynamic PNRs, resulting in a macroscopic FE to RFE transition. This domain evolution and transformation of FE to RFE transition in the present samples is schematically shown in Figure 1b. The highly dynamic PNRs induced large P_{max} and low P_r , which improved the DBS with the incorporation of BST, resulting in high energy storage density and high energy efficiency of the BNKT-BST RFEs [65]. The obtained W_{rec} and η of 0.55 BNKT-0.45 BST are comparable/superior to other lead-free RFEs and are promising for energy storage capacitors [64–69].

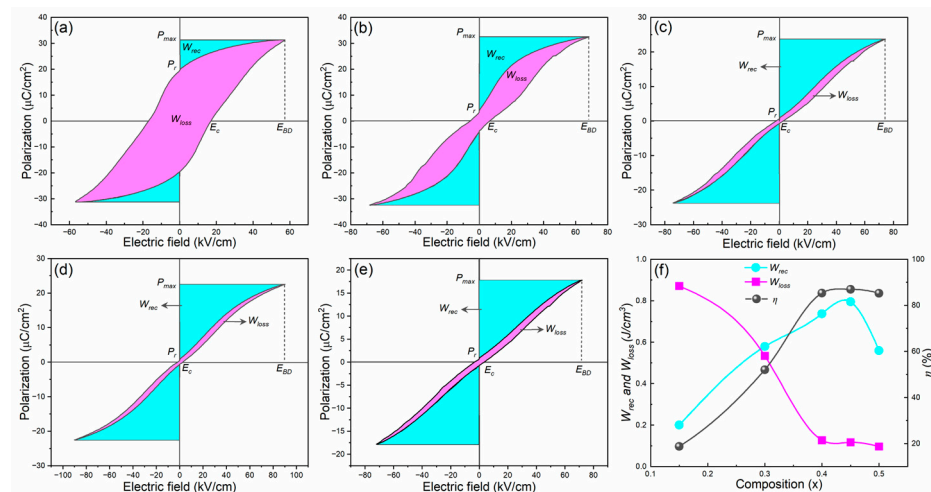


Figure 6. P - E loops of BNKT-BST ceramics measured at E_{BD} and 10 Hz for (a) $x = 0.15$, (b) $x = 0.30$, (c) $x = 0.40$, (d) $x = 0.45$, and (e) $x = 0.50$. (f) Composition (x) versus W_{rec} , W_{loss} , and η .

Electrical fatigue endurance is an important property necessary for energy storage applications. Therefore, the fatigue behavior of BNKT-BST ceramic capacitors was measured up to 10^6 electric cycles at a frequency of 10 Hz under an electric field of 90 kV/cm . Figure 7 shows the unipolar P - E loops of BNKT-BST ($x = 0.45$) and corresponding W_{rec} (square line) and η (circle line) values measured after various electric cycles (black, red and blue colour P - E loops measured at 10^0 and 10^3 and 10^6 , respectively, as shown in inset of Figure 7). It is observed that the slender P - E loops are without significant change, revealing an excellent fatigue-free response and negligible variations in W_{rec} and η .

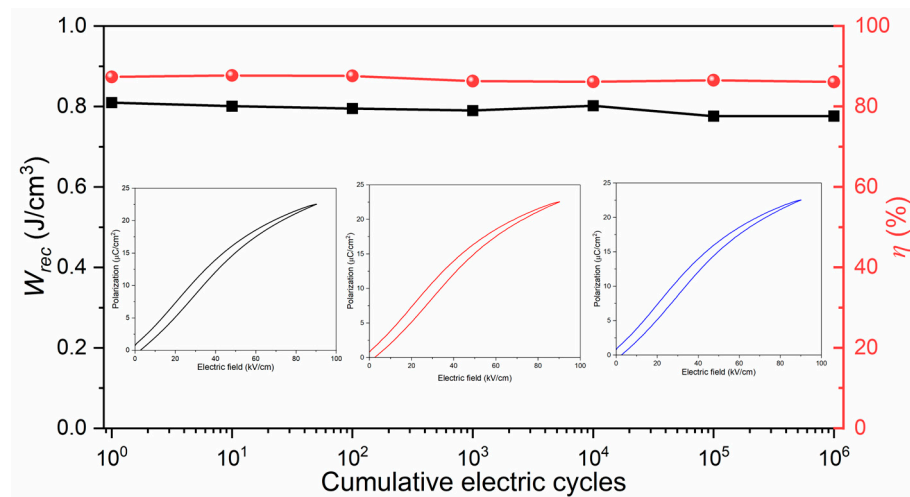


Figure 7. Fatigue behavior of BNKT-BST for $x = 0.45$ composition measured up to 10^6 electric cycles.

4. Conclusions

The domain-engineered relaxor ferroelectric BNKT-BST lead-free ceramics were fabricated by a solid-state reaction method and demonstrated structural, microstructural, dielectric, and ferroelectric properties in detail. XRD, Raman spectra, and FESEM studies revealed the formation of a rhombohedral-tetragonal phase, highly dynamic PNRs, and dense microstructure. The dielectric properties were improved with BST, and a high ϵ_r of 2664 and low $\tan \delta$ of 0.058 at 1 kHz were obtained for the $x = 0.45$ composition. The incorporation of BST into BNKT can disturb the long-range ferroelectric order, causing lowered T_m and the formation of highly dynamic PNRs. In addition, the T_m shifts toward a high temperature with frequency and diffuse phase transition, indicating relaxor ferroelectric characteristics of BNKT-BST ceramics, and is confirmed via the modified Curie-Weiss

law. The rhombohedral-tetragonal phase, fine grain size, and lowered T_m with relaxor properties simultaneously contribute to a high P_{max} and low P_r . This improves the DBS and gives rise to giant energy storage density and high energy efficiency of the BNKT-BST RFEs, making this material a good candidate for pulse-driving energy storage applications.

Author Contributions: Conceptualization, measurement, data curation, investigation, visualization, writing—original draft preparation, review, and editing, S.P.; data curation, formal analysis, H.C.; data curation, Y.L.; writing—review and editing, K.-I.P.; writing—review and editing, K.C.; validation, project administration, writing—review and editing, supervision, G.-T.H. All authors have read and agreed to the published version of the manuscript.

Funding: This research was funded by an NRF grant from the Korean government (MSIT) (no. 2022R1A2C4001497).

Institutional Review Board Statement: Not applicable.

Informed Consent Statement: Not applicable.

Data Availability Statement: Not applicable.

Conflicts of Interest: The authors declare no conflict of interest.

References

1. Shen, Y.; Zhang, X.; Li, M.; Lin, Y.; Nan, C.-W. Polymer Nanocomposite Dielectrics for Electrical Energy Storage. *Natl. Sci. Rev.* **2017**, *4*, 23–25. [[CrossRef](#)]
2. Yao, Z.; Song, Z.; Hao, H.; Yu, Z.; Cao, M.; Zhang, S.; Lanagan, M.T.; Liu, H. Homogeneous/Inhomogeneous-Structured Dielectrics and Their Energy-Storage Performances. *Adv. Mater.* **2017**, *29*, 1601727. [[CrossRef](#)]
3. Palneedi, H.; Peddigari, M.; Hwang, G.-T.; Jeong, D.-Y.; Ryu, J. High-Performance Dielectric Ceramic Films for Energy Storage Capacitors: Progress and Outlook. *Adv. Funct. Mater.* **2018**, *28*, 1803665. [[CrossRef](#)]
4. Li, Q.; Chen, L.; Gadinski, M.R.; Zhang, S.; Zhang, G.; Li, H.U.; Jagodkine, E.; Haque, A.; Chen, L.-Q.; Jackson, T.N.; et al. Flexible High-Temperature Dielectric Materials from Polymer Nanocomposites. *Nature* **2015**, *523*, 576–579. [[CrossRef](#)]
5. Kumar, N.; Ionin, A.; Ansell, T.; Kwon, S.; Hackenberger, W.; Cann, D. Multilayer Ceramic Capacitors Based on Relaxor BaTiO₃-Bi(Zn_{1/2}Ti_{1/2})O₃ for Temperature Stable and High Energy Density Capacitor Applications. *Appl. Phys. Lett.* **2015**, *106*, 252901. [[CrossRef](#)]
6. Li, J.; Li, F.; Xu, Z.; Zhang, S. Multilayer Lead-Free Ceramic Capacitors with Ultrahigh Energy Density and Efficiency. *Adv. Mater.* **2018**, *30*, 1802155. [[CrossRef](#)]
7. Chen, Q.; Shen, Y.; Zhang, S.; Zhang, Q.M. Polymer-Based Dielectrics with High Energy Storage Density. *Annu. Rev. Mater. Res.* **2015**, *45*, 433–458. [[CrossRef](#)]
8. Xie, A.; Zuo, R.; Qiao, Z.; Fu, Z.; Hu, T.; Fei, L. NaNbO₃-(Bi_{0.5}Li_{0.5})TiO₃ Lead-Free Relaxor Ferroelectric Capacitors with Superior Energy-Storage Performances via Multiple Synergistic Design. *Adv. Energy Mater.* **2021**, *11*, 2101378. [[CrossRef](#)]
9. Li, T.; Jiang, X.; Li, J.; Xie, A.; Fu, J.; Zuo, R. Ultrahigh Energy-Storage Performances in Lead-Free Na_{0.5}Bi_{0.5}TiO₃-Based Relaxor Antiferroelectric Ceramics through a Synergistic Design Strategy. *ACS Appl. Mater. Interfaces* **2022**, *14*, 22263–22269. [[CrossRef](#)]
10. Li, B.; Yan, Z.; Zhou, X.; Qi, H.; Koval, V.; Luo, X.; Luo, H.; Yan, H.; Zhang, D. Achieving Ultrahigh Energy Storage Density of La and Ta Codoped AgNbO₃ Ceramics by Optimizing the Field-Induced Phase Transitions. *ACS Appl. Mater. Interfaces* **2023**, *15*, 4246–4256. [[CrossRef](#)]
11. Yang, Z.; Du, H.; Jin, L.; Poelman, D. High-Performance Lead-Free Bulk Ceramics for Electrical Energy Storage Applications: Design Strategies and Challenges. *J. Mater. Chem A Mater.* **2021**, *9*, 18026–18085. [[CrossRef](#)]
12. Okhay, O.; Vilarinho, P.M.; Tkach, A. Structure, Microstructure, and Dielectric Response of Polycrystalline Sr_{1-x}Zn_xTiO₃ Thin Films. *Coatings* **2023**, *13*, 165. [[CrossRef](#)]
13. Pu, Y.; Wang, W.; Guo, X.; Shi, R.; Yang, M.; Li, J. Enhancing the Energy Storage Properties of Ca_{0.5}Sr_{0.5}TiO₃-Based Lead-Free Linear Dielectric Ceramics with Excellent Stability through Regulating Grain Boundary Defects. *J. Mater. Chem. C Mater.* **2019**, *7*, 14384–14393. [[CrossRef](#)]
14. Chauhan, V.; Wang, B.-X.; Ye, Z.-G. Structure, Antiferroelectricity and Energy-Storage Performance of Lead Hafnate in a Wide Temperature Range. *Materials* **2023**, *16*, 4144. [[CrossRef](#)]
15. Zhu, L.-F.; Deng, S.; Zhao, L.; Li, G.; Wang, Q.; Li, L.; Yan, Y.; Qi, H.; Zhang, B.-P.; Chen, J.; et al. Heterovalent-Doping-Enabled Atom-Displacement Fluctuation Leads to Ultrahigh Energy-Storage Density in AgNbO₃-Based Multilayer Capacitors. *Nat. Commun.* **2023**, *14*, 1166. [[CrossRef](#)] [[PubMed](#)]
16. Moradi, P.; Taheri-Nassaj, E.; Yourdkhani, A.; Mykhailovych, V.; Diaconu, A.; Rotaru, A. Enhanced Energy Storage Performance in Reaction-Sintered AgNbO₃ Antiferroelectric Ceramics. *Dalton Trans.* **2023**, *52*, 4462–4474. [[CrossRef](#)] [[PubMed](#)]
17. An, K.; Li, G.; Fan, T.; Huang, F.; Wang, W.; Wang, J. Enhanced Energy Storage Performance of AgNbO₃:XCeO₂ by Synergistic Strategies of Tolerance Factor and Density Regulations. *Coatings* **2023**, *13*, 534. [[CrossRef](#)]

18. Zhang, M.-H.; Ding, H.; Egert, S.; Zhao, C.; Villa, L.; Fulanović, L.; Groszewicz, P.B.; Buntkowsky, G.; Kleebe, H.-J.; Albe, K.; et al. Tailoring High-Energy Storage NaNbO₃-Based Materials from Antiferroelectric to Relaxor States. *Nat. Commun.* **2023**, *14*, 1525. [[CrossRef](#)] [[PubMed](#)]
19. Yang, L.; Kong, X.; Li, F.; Hao, H.; Cheng, Z.; Liu, H.; Li, J.-F.; Zhang, S. Perovskite Lead-Free Dielectrics for Energy Storage Applications. *Prog. Mater. Sci.* **2019**, *102*, 72–108. [[CrossRef](#)]
20. Gui, D.-Y.; Ma, X.-Y.; Yuan, H.-D.; Wang, C.-H. Mn- and Yb-Doped BaTiO₃-(Na_{0.5}Bi_{0.5})TiO₃ Ferroelectric Relaxor with Low Dielectric Loss. *Materials* **2023**, *16*, 2229. [[CrossRef](#)]
21. Shi, H.; Li, K.; Li, F.; Ma, J.; Tu, Y.; Long, M.; Lu, Y.; Gong, W.; Wang, C.; Shan, L. Enhanced Piezoelectricity and Thermal Stability of Electrostrain Performance in BiFeO₃-Based Lead-Free Ceramics. *Nanomaterials* **2023**, *13*, 942. [[CrossRef](#)]
22. Ji, H.; Wang, D.; Bao, W.; Lu, Z.; Wang, G.; Yang, H.; Mostaed, A.; Li, L.; Feteira, A.; Sun, S.; et al. Ultrahigh Energy Density in Short-Range Tilted NBT-Based Lead-Free Multilayer Ceramic Capacitors by Nanodomain Percolation. *Energy Storage Mater.* **2021**, *38*, 113–120. [[CrossRef](#)]
23. Zhang, G.; Zhu, D.; Zhang, X.; Zhang, L.; Yi, J.; Xie, B.; Zeng, Y.; Li, Q.; Wang, Q.; Jiang, S. High-Energy Storage Performance of (Pb_{0.87} Ba_{0.1} La_{0.02})(Zr_{0.68} Sn_{0.24} Ti_{0.08})O₃ Antiferroelectric Ceramics Fabricated by the Hot-Press Sintering Method. *J. Am. Ceram. Soc.* **2015**, *98*, 1175–1181. [[CrossRef](#)]
24. Liu, Z.; Chen, X.; Peng, W.; Xu, C.; Dong, X.; Cao, F.; Wang, G. Temperature-Dependent Stability of Energy Storage Properties of Pb_{0.97} La_{0.02} (Zr_{0.58} Sn_{0.335} Ti_{0.085})O₃ Antiferroelectric Ceramics for Pulse Power Capacitors. *Appl. Phys. Lett.* **2015**, *106*, 262901. [[CrossRef](#)]
25. Yuan, Q.; Li, G.; Yao, F.-Z.; Cheng, S.-D.; Wang, Y.; Ma, R.; Mi, S.-B.; Gu, M.; Wang, K.; Li, J.-F.; et al. Simultaneously Achieved Temperature-Insensitive High Energy Density and Efficiency in Domain Engineered BaTiO₃-Bi(Mg_{0.5}Zr_{0.5})O₃ Lead-Free Relaxor Ferroelectrics. *Nano Energy* **2018**, *52*, 203–210. [[CrossRef](#)]
26. Zhao, P.; Wang, H.; Wu, L.; Chen, L.; Cai, Z.; Li, L.; Wang, X. High-Performance Relaxor Ferroelectric Materials for Energy Storage Applications. *Adv. Energy Mater.* **2019**, *9*, 1803048. [[CrossRef](#)]
27. Asbani, B.; Gagou, Y.; Ben Moumen, S.; Dellis, J.-L.; Lahmar, A.; Amjoud, M.; Mezzane, D.; El Marssi, M.; Rozic, B.; Kutnjak, Z. Large Electrocaloric Responsivity and Energy Storage Response in the Lead-Free Ba(GexTi1-x)O₃ Ceramics. *Materials* **2022**, *15*, 5227. [[CrossRef](#)]
28. Yin, J.; Zhang, Y.; Lv, X.; Wu, J. Ultrahigh Energy-Storage Potential under Low Electric Field in Bismuth Sodium Titanate-Based Perovskite Ferroelectrics. *J. Mater. Chem. A Mater.* **2018**, *6*, 9823–9832. [[CrossRef](#)]
29. Qi, H.; Zuo, R. Linear-like Lead-Free Relaxor Antiferroelectric (Bi_{0.5} Na_{0.5})TiO₃-NaNbO₃ with Giant Energy-Storage Density/Efficiency and Super Stability against Temperature and Frequency. *J. Mater. Chem. A Mater.* **2019**, *7*, 3971–3978. [[CrossRef](#)]
30. Lu, Y.; Zhang, H.; Yang, H.; Fan, P.; Samart, C.; Takesue, N.; Tan, H. SPS-Prepared High-Entropy (Bi_{0.2}Na_{0.2}Sr_{0.2}Ba_{0.2}Ca_{0.2})TiO₃ Lead-Free Relaxor-Ferroelectric Ceramics with High Energy Storage Density. *Crystals* **2023**, *13*, 445. [[CrossRef](#)]
31. Jiang, Y.; Niu, X.; Liang, W.; Jian, X.; Shi, H.; Li, F.; Zhang, Y.; Wang, T.; Gong, W.; Zhao, X.; et al. Enhanced Energy Storage Performance in Na_{0.5}Bi_{0.5}TiO₃-Based Relaxor Ferroelectric Ceramics via Compositional Tailoring. *Materials* **2022**, *15*, 5881. [[CrossRef](#)] [[PubMed](#)]
32. Wang, G.; Li, J.; Zhang, X.; Fan, Z.; Yang, F.; Feteira, A.; Zhou, D.; Sinclair, D.C.; Ma, T.; Tan, X.; et al. Ultrahigh Energy Storage Density Lead-Free Multilayers by Controlled Electrical Homogeneity. *Energy Env. Sci.* **2019**, *12*, 582–588. [[CrossRef](#)]
33. Pan, H.; Li, F.; Liu, Y.; Zhang, Q.; Wang, M.; Lan, S.; Zheng, Y.; Ma, J.; Gu, L.; Shen, Y.; et al. Ultrahigh-Energy Density Lead-Free Dielectric Films via Polymorphic Nanodomain Design. *Science* **2019**, *365*, 578–582. [[CrossRef](#)]
34. Yang, Z.; Wang, B.; Li, Y.; Hall, D.A. Enhancement of Nonlinear Dielectric Properties in BiFeO₃-BaTiO₃ Ceramics by Nb-Doping. *Materials* **2022**, *15*, 2872. [[CrossRef](#)]
35. Wang, D.; Liu, J.; Zeng, M.; Zhang, C.; Li, H.; Yu, H.; Yuan, Y.; Zhang, S. Stabilizing Temperature-capacitance Dependence of (Sr, Pb, Bi)TiO₃-Bi₄Ti₃O₁₂ Solutions for Energy Storage. *J. Am. Ceram. Soc.* **2019**, *102*, 4029–4037. [[CrossRef](#)]
36. Wendari, T.P.; Zulfadjri. Emriadi Observation of Relaxor Ferroelectric Behavior and Energy Storage Performances in Sr_{1.25}Bi_{2.75}Nb_{1.25}Ti_{1.75}O₁₂ Aurivillius Ceramic Synthesized by Molten Salt Method. *J. Solid State Chem.* **2023**, *325*, 124150. [[CrossRef](#)]
37. Luo, C.; Zheng, X.; Zheng, P.; Du, J.; Niu, Z.; Zhang, K.; Bai, W.; Fan, Q.; Zheng, L.; Zhang, Y. Realizing Excellent Energy Storage Performances in Tetragonal Tungsten Bronze Ceramics via a B-Site Engineering Strategy. *J. Alloys Compd.* **2023**, *933*, 167809. [[CrossRef](#)]
38. Li, F.; Hou, X.; Wang, J.; Zeng, H.; Shen, B.; Zhai, J. Structure-Design Strategy of 0-3 Type (Bi_{0.32}Sr_{0.42}Na_{0.20})TiO₃/MgO Composite to Boost Energy Storage Density, Efficiency and Charge-Discharge Performance. *J. Eur. Ceram. Soc.* **2019**, *39*, 2889–2898. [[CrossRef](#)]
39. Liu, N.; Liang, R.; Zhou, Z.; Dong, X. Designing Lead-Free Bismuth Ferrite-Based Ceramics Learning from Relaxor Ferroelectric Behavior for Simultaneous High Energy Density and Efficiency under Low Electric Field. *J. Mater. Chem. C Mater.* **2018**, *6*, 10211–10217. [[CrossRef](#)]
40. Wu, Y.; Fan, Y.; Liu, N.; Peng, P.; Zhou, M.; Yan, S.; Cao, F.; Dong, X.; Wang, G. Enhanced Energy Storage Properties in Sodium Bismuth Titanate-Based Ceramics for Dielectric Capacitor Applications. *J. Mater. Chem. C Mater.* **2019**, *7*, 6222–6230. [[CrossRef](#)]
41. Hu, Q.; Tian, Y.; Zhu, Q.; Bian, J.; Jin, L.; Du, H.; Alikin, D.O.; Shur, V.Y.; Feng, Y.; Xu, Z.; et al. Achieve Ultrahigh Energy Storage Performance in BaTiO₃-Bi(Mg_{1/2}Ti_{1/2})O₃ Relaxor Ferroelectric Ceramics via Nano-Scale Polarization Mismatch and Reconstruction. *Nano Energy* **2020**, *67*, 104264. [[CrossRef](#)]

42. Sayyed, S.; Acharya, S.A.; Kautkar, P.; Sathe, V. Structural and Dielectric Anomalies near the MPB Region of $\text{Na}_{0.5}\text{Bi}_{0.5}\text{TiO}_3\text{-SrTiO}_3$ Solid Solution. *RSC Adv.* **2015**, *5*, 50644–50654. [[CrossRef](#)]
43. Ma, W.; Zhu, Y.; Marwat, M.A.; Fan, P.; Xie, B.; Salamon, D.; Ye, Z.-G.; Zhang, H. Enhanced Energy-Storage Performance with Excellent Stability under Low Electric Fields in BNT-ST Relaxor Ferroelectric Ceramics. *J. Mater. Chem. C Mater.* **2019**, *7*, 281–288. [[CrossRef](#)]
44. Shi, L.N.; Wang, Y.G.; Ren, Z.H.; Jain, A.; Jiang, S.S.; Chen, F.G. Significant Improvement in Electrical Characteristics and Energy Storage Performance of NBT-Based Ceramics. *Ceram. Int.* **2022**, *48*, 26973–26983. [[CrossRef](#)]
45. Kong, X.; Yang, L.; Cheng, Z.; Zhang, S. Bi-modified SrTiO_3 -based Ceramics for High-temperature Energy Storage Applications. *J. Am. Ceram. Soc.* **2020**, *103*, 1722–1731. [[CrossRef](#)]
46. Wei, T.; Liu, K.; Fan, P.; Lu, D.; Ye, B.; Zhou, C.; Yang, H.; Tan, H.; Salamon, D.; Nan, B.; et al. Novel $\text{NaNbO}_3\text{-Sr}_{0.7}\text{Bi}_{0.2}\text{TiO}_3$ Lead-Free Dielectric Ceramics with Excellent Energy Storage Properties. *Ceram. Int.* **2021**, *47*, 3713–3719. [[CrossRef](#)]
47. Pham, K.-N.; Hussain, A.; Ahn, C.W.; Kim, W.; Jeong, S.J.; Lee, J.-S. Giant Strain in Nb-Doped $\text{Bi}_{0.5}(\text{Na}_{0.82}\text{K}_{0.18})_{0.5}\text{TiO}_3$ Lead-Free Electromechanical Ceramics. *Mater. Lett.* **2010**, *64*, 2219–2222. [[CrossRef](#)]
48. Pattipaka, S.; James, A.R.; Dobbidi, P. Dielectric, Piezoelectric and Variable Range Hopping Conductivity Studies of $\text{Bi}_{0.5}(\text{Na}, \text{K})_{0.5}\text{TiO}_3$ Ceramics. *J. Electron. Mater.* **2018**, *47*, 3876–3890. [[CrossRef](#)]
49. Ullah, A.; Ahn, C.W.; Hussain, A.; Lee, S.Y.; Kim, J.S.; Kim, I.W. Effect of Potassium Concentration on the Structure and Electrical Properties of Lead-Free $\text{Bi}_{0.5}(\text{Na}, \text{K})_{0.5}\text{TiO}_3\text{-BiAlO}_3$ Piezoelectric Ceramics. *J. Alloys Compd.* **2011**, *509*, 3148–3154. [[CrossRef](#)]
50. Sumang, R.; Cann, D.P.; Kumar, N.; Bongkarn, T. Large Strain in Lead-Free Piezoelectric $(1-x-y)\text{Bi}_{0.5}\text{Na}_{0.5}\text{TiO}_3\text{-xBi}_{0.5}\text{K}_{0.5}\text{TiO}_3\text{-YBi}_{0.5}\text{Li}_{0.5}\text{TiO}_3$ System near MPB Prepared via the Combustion Technique. *Ceram. Int.* **2015**, *41*, S127–S135. [[CrossRef](#)]
51. Fernandez-Benavides, D.; Gutierrez-Perez, A.; Benitez-Castro, A.; Ayala-Ayala, M.; Moreno-Murguía, B.; Muñoz-Saldaña, J. Comparative Study of Ferroelectric and Piezoelectric Properties of BNT-BKT-BT Ceramics near the Phase Transition Zone. *Materials* **2018**, *11*, 361. [[CrossRef](#)] [[PubMed](#)]
52. Gupta, S.K.; McQuade, R.; Gibbons, B.; Mardilovich, P.; Cann, D.P. Electric Field-Induced Strain in $\text{Sr}(\text{Hf}_{0.5}\text{Zr}_{0.5})\text{O}_3$ -Modified $\text{Bi}_{0.5}(\text{Na}_{0.8}\text{K}_{0.2})_{0.5}\text{TiO}_3$ Piezoelectric Ceramics. *J. Appl. Phys.* **2020**, *127*, 074104. [[CrossRef](#)]
53. Pattipaka, S.; James, A.R.; Dobbidi, P. Enhanced Dielectric and Piezoelectric Properties of BNT-KNNG Piezoelectric Ceramics. *J. Alloys Compd.* **2018**, *765*, 1195–1208. [[CrossRef](#)]
54. Tong, X.-Y.; Song, M.-W.; Zhou, J.-J.; Wang, K.; Guan, C.-L.; Liu, H.; Fang, J.-Z. Enhanced Energy Storage Properties in Nb-Modified $\text{Bi}_{0.5}\text{Na}_{0.5}\text{TiO}_3\text{-SrTiO}_3$ Lead-Free Electroceramics. *J. Mater. Sci. Mater. Electron.* **2019**, *30*, 5780–5790. [[CrossRef](#)]
55. Jaita, P.; Saenkam, K.; Rujijanagul, G. Improvements in Piezoelectric and Energy Harvesting Properties with a Slight Change in Depolarization Temperature in Modified BNKT Ceramics by a Simple Technique. *RSC Adv.* **2023**, *13*, 3743–3758. [[CrossRef](#)]
56. Chu, B.; Hao, J.; Li, P.; Li, Y.; Li, W.; Zheng, L.; Zeng, H. High-Energy Storage Properties over a Broad Temperature Range in La-Modified BNT-Based Lead-Free Ceramics. *ACS Appl. Mater. Interfaces* **2022**, *14*, 19683–19696. [[CrossRef](#)]
57. Jaita, P.; Watcharapasorn, A.; Cann, D.P.; Jiansirisomboon, S. Dielectric, Ferroelectric and Electric Field-Induced Strain Behavior of $\text{Ba}(\text{Ti}_{0.90}\text{Sn}_{0.10})\text{O}_3$ -Modified $\text{Bi}_{0.5}(\text{Na}_{0.80}\text{K}_{0.20})_{0.5}\text{TiO}_3$ Lead-Free Piezoelectrics. *J. Alloys Compd.* **2014**, *596*, 98–106. [[CrossRef](#)]
58. Zhang, H.; Zhou, J.; Shen, J.; Yang, X.; Wu, C.; Han, K.; Zhao, Z.; Chen, W. Enhanced Piezoelectric Property and Promoted Depolarization Temperature in Fe Doped $\text{Bi}_{1/2}(\text{Na}_{0.8}\text{K}_{0.2})_{1/2}\text{TiO}_3$ Lead-Free Ceramics. *Ceram. Int.* **2017**, *43*, 16395–16402. [[CrossRef](#)]
59. Huang, Y.; Zhao, C.; Wu, B.; Wu, J. Multifunctional BaTiO_3 -Based Relaxor Ferroelectrics toward Excellent Energy Storage Performance and Electrostrictive Strain Benefiting from Crossover Region. *ACS Appl. Mater. Interfaces* **2020**, *12*, 23885–23895. [[CrossRef](#)]
60. Sun, Z.; Wang, Z.; Tian, Y.; Wang, G.; Wang, W.; Yang, M.; Wang, X.; Zhang, F.; Pu, Y. Progress, Outlook, and Challenges in Lead-Free Energy-Storage Ferroelectrics. *Adv. Electron. Mater* **2020**, *6*, 1900698. [[CrossRef](#)]
61. Shvartsman, V.V.; Lupascu, D.C. Lead-Free Relaxor Ferroelectrics. *J. Am. Ceram. Soc.* **2012**, *95*, 1–26. [[CrossRef](#)]
62. Liu, G.; Wang, Y.; Han, G.; Gao, J.; Yu, L.; Tang, M.; Li, Y.; Hu, J.; Jin, L.; Yan, Y. Enhanced Electrical Properties and Energy Storage Performances of NBT-ST Pb-Free Ceramics through Glass Modification. *J. Alloys Compd.* **2020**, *836*, 154961. [[CrossRef](#)]
63. Uchino, K.; Nomura, S.; Cross, L.E.; Jang, S.J.; Newnham, R.E. Electrostrictive Effect in Lead Magnesium Niobate Single Crystals. *J. Appl. Phys.* **1980**, *51*, 1142–1145. [[CrossRef](#)]
64. Li, Q.; Wang, C.; Yadav, A.K.; Fan, H. Large Electrostrictive Effect and Energy Storage Density in MnCO_3 Modified $\text{Na}_{0.325}\text{Bi}_{0.395}\text{Sr}_{0.245}\text{TiO}_3$ Lead-Free Ceramics. *Ceram. Int.* **2020**, *46*, 3374–3381. [[CrossRef](#)]
65. Wu, J.; Mahajan, A.; Riekehr, L.; Zhang, H.; Yang, B.; Meng, N.; Zhang, Z.; Yan, H. Perovskite $\text{Sr}_x(\text{Bi}_{1-x}\text{Na}_{0.97-x}\text{Li}_{0.03})_{0.5}\text{TiO}_3$ Ceramics with Polar Nano Regions for High Power Energy Storage. *Nano Energy* **2018**, *50*, 723–732. [[CrossRef](#)]
66. Yan, Y.; Zeng, X.; Deng, T.; Chen, F.; Yang, L.; He, Z.; Jin, L.; Liu, G. Rheological, Mechanical, and Electrical Properties of $\text{Sr}_{0.7}\text{Bi}_{0.2}\text{TiO}_3$ Modified BaTiO_3 Ceramic and Its Composites. *J. Am. Ceram. Soc.* **2023**, *106*, 3052–3065. [[CrossRef](#)]
67. Nayak, S.; Venkateswarlu, S.; Budisuharto, A.S.; Jørgensen, M.R.V.; Borkiewicz, O.; Beyer, K.A.; Pramanick, A. Effect of A-site Substitutions on Energy Storage Properties of $\text{BaTiO}_3\text{-BiScO}_3$ Weakly Coupled Relaxor Ferroelectrics. *J. Am. Ceram. Soc.* **2019**, *102*, 5919–5933. [[CrossRef](#)]

68. Cao, W.P.; Li, W.L.; Dai, X.F.; Zhang, T.D.; Sheng, J.; Hou, Y.F.; Fei, W.D. Large Electrocaloric Response and High Energy-Storage Properties over a Broad Temperature Range in Lead-Free NBT-ST Ceramics. *J. Eur. Ceram. Soc.* **2016**, *36*, 593–600. [[CrossRef](#)]
69. Jabeen, N.; Hussain, A.; Qaiser, M.A.; Ali, J.; Rehman, A.; Sfina, N.; Ali, G.A.; Tirth, V. Enhanced Energy Storage Performance by Relaxor Highly Entropic $(\text{Ba}_{0.2}\text{Na}_{0.2}\text{K}_{0.2}\text{La}_{0.2}\text{Bi}_{0.2})\text{TiO}_3$ and $(\text{Ba}_{0.2}\text{Na}_{0.2}\text{K}_{0.2}\text{Mg}_{0.2}\text{Bi}_{0.2})\text{TiO}_3$ Ferroelectric Ceramics. *Appl. Sci.* **2022**, *12*, 12933. [[CrossRef](#)]

Disclaimer/Publisher's Note: The statements, opinions and data contained in all publications are solely those of the individual author(s) and contributor(s) and not of MDPI and/or the editor(s). MDPI and/or the editor(s) disclaim responsibility for any injury to people or property resulting from any ideas, methods, instructions or products referred to in the content.